Molecular Dynamics Simulations of Matrix Metalloproteinase 2: Role of the Structural Metal Ions[†,‡]

Natalia Díaz* and Dimas Suárez

Departamento de Química Física y Analítica, Universidad de Oviedo, C/Julián Clavería, 8. 33006, Oviedo (Asturias), Spain

Received March 20, 2007; Revised Manuscript Received May 30, 2007

ABSTRACT: Herein we investigate the role played by the so-called "structural metal ions" in the catalytic domain of the matrix metalloproteinase 2 enzyme (MMP-2 or gelatinase A). We performed seven molecular dynamics simulations that differ in the number and position of the noncatalytic zinc and calcium ions bound to the MMP-2 catalytic domain. An additional simulation including the three fibronectin-type modules inserted into the catalytic domain was also carried out. The analysis of the trajectories confirms that the binding/removal of the structural ions does not perturb the secondary structure elements but influences the position of several solvent-exposed loop regions that are placed near the active site cleft. The position of these loops modulates the accessibility of important anchorage points for substrate binding that have been identified in the active site groove. On the basis of semiempirical quantum chemical calculations, we estimated the relative free energies of the MMP-2 models, obtaining thus that the binding of two zinc and two calcium ions to the MMP-2 catalytic domain is energetically favored. In this MMP-2 model, which shows the most compact structure, all of the substrate binding sites are readily accessible. Globally, our results help to rationalize at the atomic level the calcium and zinc dependence of the hydrolytic activity catalyzed by the MMPs.

Matrix metalloproteinases (MMPs),[1] a family of zinc- and calcium-dependent endopeptidases, are involved in important physiological processes including tissue remodeling and repair (*1, 2*). However, their expression is also known to increase in various inflammatory, malignant, and degenerative diseases, and accordingly, the MMPs are considered as targets for drug design (*3*−*5*). Structurally, the MMPs are multidomain enzymes formed, in most cases, by an N-terminal prodomain, a catalytic domain, and a C-terminal hemopexin-like domain (*6*−*8*). The rational design of inhibitors has focused in the catalytic domain, which is formed by a twisted five-stranded β-sheet, three α-helices, and several bridging loops. In gelatinases (e.g., MMP-2), the catalytic domain has three fibronectin-related modules inserted into the sequence between strand β5 and helix α2. The active site, located in the catalytic domain, contains a conserved zinc binding motif (HEXXHXXGXXH) responsible for coordinating the catalytic zinc ion (Zn_1). It also includes a conserved glutamate residue that is critical for catalysis as revealed by mutagenesis experiments (*9*, *10*).

The MMPs appear to be unique among the metalloendopeptidases in that they seem to contain an additional zinc atom (Zn_2) of unknown function. Initially, direct metal analysis performed for several enzymes (MMP-1, MMP-2, MMP-3, and MMP-7) provided confusing results with zinc stoichiometries that varied between 1 and 2 metal atoms per enzyme molecule (*11*−*14*). However, it was later found that the zinc content depends on the purification procedure and on the method for sample preparation (*13*). Nevertheless, the relevance of the second zinc binding site has been highlighted by mutagenesis experiments, showing that a double substitution in the Zn_2 coordination sphere of MMP-1 resulted in a dramatic reduction of proteolytic activity (*15*). Crystallographic data available for several MMPs provide further evidence for the binding of two zinc ions in the catalytic domain of these enzymes (*8*). The structures show that Zn_1 is coordinated by the three conserved histidine residues (located in α2 and the Ω loop) and by one or two water molecules, while Zn_2 is liganded in a tetrahedral coordination sphere made up by three histidines (from the long S-loop and β4- and β5-strands, respectively) and one aspartic acid (from the S-loop) (*8*). Sequence alignment and homology modeling performed for the catalytic domains of the entire MMP family revealed that the MMPs could have developed at least four different motifs for binding to the Zn_2 metal ion (*16*, *17*).

The catalytic domain of the MMPs can also bind a number of calcium ions that are essential for the folding, the stability, and the catalytic activity of the enzymes. Thus, removal of Ca^{2+} from the full-length MMP-1 generates a catalytically incompetent enzyme (*18*). A similar calcium-dependent activity has also been observed for MMP-3 (*19*). Intriguingly,

[†] This research was supported by the Spanish MEC via the "Ramon y Cajal" program and Grant CTQ2004−06309.

[‡] This paper is dedicated to the memory of Professor Lorenzo Pueyo.

* To whom corresponcence should be addressed. Phone: +34-985103492. Fax: +34-985103125. E-mail: diazfnatalia@uniovi.es.

[1] Abbreviations: MMP, matrix metalloproteinase; DC, divide and conquer; DFT, density functional theory; MD, molecular dynamics; QM, quantum mechanical; QM/MM, hybrid quantum mechanical and molecular mechanical; PB, Poisson−Boltzmann; NMR, nuclear magnetic resonance; PDB, Protein Data Bank; SASA, solvent-accessible surface area; MM-PBSA, molecular mechanics−Poisson−Boltzmann surface area; QM-PBSA, quantum mechanics−Poisson−Boltzmann surface area.

10.1021/bi700541p CCC: $37.00
Published on Web 07/07/2007

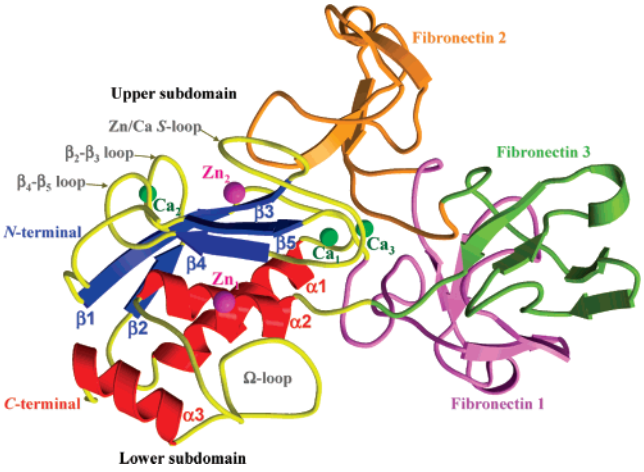

FIGURE 1: Crystal structure (1CK7) of the catalytic domain of the MMP-2 enzyme showing the main structural elements and the binding sites for the zinc (in magenta) and calcium (in green) ions. The three fibronectin-type domains are also displayed.

circular dichroism (CD) spectra indicate that dissociation of Zn^{2+} and Ca^{2+} from the catalytic domain of MMP-1 and MMP-3 produces no global changes in the secondary structure of the enzymes, whereas fluorescence emission experiments suggest that removal of calcium results in a partially unfolded state characterized by the exposure of at least one tryptophyl residue to a more polar environment (*19*, *20*). In addition, Ca^{2+} ions seem to stabilize a compact protein structure that is less susceptible to denaturation and proteolysis (*19*, *21*).

Crystallographic analyses have revealed that the catalytic domain of the MMPs can bind one to three calcium ions. One of these calcium binding sites (Ca_1) is located close to the Zn_2 site. Both Zn_2 and Ca_1 link the long S-shaped double loop with the β-sheet (see Figure 1). A second calcium ion (Ca_2) is sandwiched between the $\beta2-\beta3$ and the $\beta4-\beta5$ connecting loops, whereas the loop following strand $\beta5$ encircles a third calcium atom (Ca_3) in some crystal structures (*8*). Thus, it has been proposed that the noncatalytic zinc and calcium ions could play a structural role by stabilizing important loop regions of the catalytic domain, and accordingly, they are termed the "structural metal ions". However, the precise structural basis for zinc and calcium stabilization remains largely unknown because a three-dimensional model of a metal-free enzyme is not yet available for comparison.

In this work, we investigated the role played by the Zn_2 and Ca_1-Ca_3 ions in the structure and stability of the catalytic domain of the MMP-2 enzyme (gelatinase A). The crystal structures available for this enzyme correspond to the full-length human pro-MMP-2 (two structures) and to the catalytic domain with the fibronectin-like modules deleted (two structures) (*22*−*24*). In addition, a three-dimensional structure of the catalytic domain of MMP-2 has been derived by nuclear magnetic resonance (NMR) methods (*25*). Altogether, these structures show that the catalytic domain is unaffected by the insertion of the fibronectin-like motifs or by the presence of the propeptide. Concerning the metal ions, the different MMP-2 structures display two zinc ions bound in the Zn_1 and Zn_2 sites. However, they differ in the number of calcium ions: one Ca^{2+} ion (Ca_1) for the full-length pro-MMP-2/TIMP-2 complex (PDB Id code 1GXD, 3.1 Å of resolution), (*24*) two (Ca_1 and Ca_2) for the full-length pro-MMP-2, (1CK7, 2.8 Å), (*23*) two (Ca_1 and Ca_2) for the Gln404Glu mutant of the catalytic domain (1EAK, 2.66 Å), two (Ca_1 and Ca_2) for the NMR models in aqueous solution (1HOV) (*25*), and three (Ca_1, Ca_2, and Ca_3) for the MMP-2 catalytic domain (1QIB, 2.8 Å) (*22*). To complement the structural information and to increase our knowledge about the structural role played by the Ca_1, Ca_2, Ca_3, and Zn_2 ions in the MMP-2 enzyme, we characterized a family of protein configurations that differ in the number and location of the metal ions bound to the enzyme by carrying out a series of molecular dynamics (MD) simulations followed by semiempirical quantum chemical calculations. All of these computational results are used to characterize the structural and dynamical influence of the metal ions as well as to predict the relative stability of the different MMP-2 configurations.

MATERIALS AND METHODS

Setup of the Systems. Initial coordinates for the MMP-2 catalytic domain were taken from the 1CK7 crystal structure, which corresponds to the Ala404Glu mutant of the full-length pro-MMP-2 enzyme (residue numbering as in the 1CK7 structure) (*23*). The propeptide ($Pro_{31}-Tyr_{110}$) and the C-terminal hemopexin domain ($Leu_{461}-Cys_{660}$) were deleted from the initial crystal structure, and the three fibronectin-type domains ($Glu_{217}-Gln_{393}$) that characterize gelatinases were replaced by a short peptide segment (Lys-Gly-Val). The ionizable residues were set to their normal ionization states at pH 7. Concerning the metal ions observed in the 1CK7 structure, the catalytic Zn_1 ion was kept in all of the MD simulations. The rest of the metal ions, Zn_2 and Ca_1-Ca_2, were successively removed to build up six enzyme configurations ($Ca_{1-2}\&Zn_{1-2}$, $Ca_2\&Zn_{1-2}$, $Ca_1\&Zn_{1-2}$, Zn_{1-2}, $Ca_{1-2}\&Zn_1$, and Zn_1) that differ in the number and/or location of the structural ions. We further considered two additional models: the seventh model is characterized by the presence of a third calcium ion, $Ca_{1-3}\&Zn_{1-2}$, as observed in the 1QIB crystal structure (*22*). Besides the Zn_2, Ca_1, and Ca_2 ions, the last model, $Ca_{1-2}\&Zn_{1-2}$-fibronectin, includes three fibronectin-type domains as in the initial crystal structure.

The resulting structures were surrounded by a periodic box of TIP3P water molecules that extended 15 Å from the protein atoms, and Na^+ counterions were placed to neutralize the systems. This resulted in a total of 2527 protein atoms being solvated by ~11500 water molecules in the different configurations of the MMP-2 catalytic domain. The parm98 version of the all-atom AMBER force field was used to model the systems (*26*). For the calcium ions, we employed the nonbonded representation proposed by Aqvist (*27*). For the zinc ions, we developed a bonded representation which places explicit bonds between the metal and the coordinating atoms (see Supporting Information for details).

Energy minimizations and MD simulations were carried out using the SANDER and the PMEMD programs included in the AMBER 8.0 suite of programs (*28*). The solvent molecules and counterions were initially relaxed by means of energy minimizations and 50 ps of MD. Subsequently, the full systems were minimized to remove bad contacts in the initial geometry and heated to 300 K during 60 ps of MD. The SHAKE algorithm was employed to constrain all R−H bonds, and periodic boundary conditions were applied

to simulate a continuous system. A nonbonded cutoff of 10.0 Å was used whereas the particle-mesh-Ewald (PME) was employed to include the contributions of long-range interactions (*29*). The pressure (1 atm) and the temperature (300 K) of the system were controlled during the MD simulations by Berendsen's method (*30*). A 10 ns trajectory was computed for each model with a time step of 2 fs, but only the last 8.0 ns of each trajectory was analyzed (coordinates were saved for analysis every 1 ps). The solvent-accessible surface area (SASA) of the MMP-2 systems was computed using the MSMS program (*31*).

Accessibility of the Peptide Anchorage Points. We computed the radii of accessibility (r_{acc}) (*32*, *33*) for several atomic groups of the MMP-2 enzyme in order to investigate the accessibility of the peptide-anchoring subsites and catalytic residues located at the active site cleft. For each atom or group of atoms, r_{acc} is defined as the maximum radius of a spherical ligand that can touch the desired target. The MSMS program (*31*) was used to carry out fast computations of molecular surfaces considering only the enzyme's heavy atoms and a probe sphere of a given radius. The van der Waals radii for the atoms were taken from the united-atom AMBER-84 force field (*34*). The output from the MSMS program was examined to determine whether the "external" molecular surface generated by the probe radius did or did not reach the desired functional group(s). We performed binary search iterations to achieve a precision of 0.05 Å in the computed values of the radii of accessibility. The r_{acc} values were calculated for a subset of snapshots taken every 80 ps along the simulations.

It is commonly assumed that the S_1' binding site in the MMPs corresponds to a flexible pocket that can accommodate hydrophobic side chains of inhibitor or substrate molecules of varying size. In the case of the MMP-2 enzyme, however, the S_1' site forms a "channel" (*35*, *36*). The main entrance to the S_1' channel is constituted by several residues located in the Zn_1 site (e.g., His_{403}, Pro_{423}, Tyr_{425}) while the S_1' "backdoor" is defined by the carbonyl group of Ala_{419} and the side chains of other residues located along the Ω-loop. To better characterize the accessibility of the S_1' site, we employed the following protocol (*33*). First, we computed an external molecular surface that blocked the two entrances to the S_1' channel using an arbitrary 2.5 Å probe radius. Second, the vertex points located on the external surface were transformed into a set of partially overlapping spheres of varying radii, which were added to the set of spheres representing the protein atoms. In this way, the catalytic domain of the MMP-2 enzyme was effectively encapsulated by the "blocking" spheres. Then we computed the size of the probe radius that can produce a continuous surface from outside the encapsulated protein to the side chain of the Val_{400} residue (which is located inside the S_1' site) passing through the two alternative S_1' doors: the main door located in the active site groove and the backdoor delineated by residues from the Ω-loop. In these analyses, some of the blocking spheres constituting the external surface in the vicinity of the corresponding alternative door had to be removed so as to allow passage of the probe sphere.

Electrostatic Calculations. The electrostatic potential of the MMP-2 models in solution was computed on selected snapshots from the MD trajectories by means of the program Delphi (*37*, *38*). The linearized Poisson−Bolztmann (PB) equation was solved on a cubic lattice by using an iterative finite-difference method (1000 iterations) and a grid spacing of 0.5 Å. Because of the small size of hydrogens in the AMBER force field, the van der Waals surface used in the PB calculations was constructed using DREIDING van der Waals radii for C, H, N, O, and S atoms (*39*). The dielectric boundary was the contact surface between the radii of the solute and the radius (1.4 Å) of a water probe molecule. The Debye−Huckel approximation was used to determine the potentials at the boundary of the grid. The electrostatic potential was plotted onto the molecular surface computed by the MSMS program.

Energetic Analyses of the MD Trajectories. To calculate the average free energies for the simulated MMP-2 configurations, we employed a variant of the so-called MM-PBSA approach (*40*, *41*) in which the enthalpy and solvation energy terms are computed by means of semiempirical QM calculations (QM-PBSA calculations). Most of the QM-PBSA computational details have been previously described (*42*, *43*), and therefore, they are briefly summarized herein.

First, a set of 50 representative snapshots were extracted every 160 ps along the last 8 ns of the simulation time of each MD trajectory. The solvated systems were subjected to MM energy minimization using a variant of the AMBER force field parameter set that has been optimized to reproduce the geometry of proteins minimized at the PM3 semiempirical quantum mechanical level (*44*). In this way, the relaxed geometries are more consistent with a semiempirical QM treatment of protein structures. From the MM relaxed structures, the coordinates of the water molecules and counterions were removed, and the average free energy of the MMP-2 models was estimated according to the equation:

$$\bar{G} \approx \bar{H}_{QM} + \bar{E}_{disp} + \Delta\bar{G}_{solv} \quad (1)$$

where $\bar{G}$ is the calculated average free energy, $\bar{H}_{QM}$ is the average QM heat of formation of the solute that accounts for intraprotein effects, $\bar{E}_{disp}$ is an empirical energy that takes into account the attractive dispersive interactions, and $\Delta\bar{G}_{solv}$ is the average solvation energy, which is calculated using a QM Hamiltonian coupled with a continuum model. Note that solute entropic contributions are not taken into account in eq 1.

The semiempirical QM energy terms in eq 1 are computed efficiently on systems containing thousands of atoms by using the divide and conquer (DC) SCF algorithm (*45*) as implemented in the DIVCON program (*46*, *47*). We performed single-point PM3 calculations using the new PM3 parameter set for Zn, which shows an improved effectiveness in modeling zinc in biological environments (*48*, *49*). Solvent effects were included within the semiempirical QM methodology by merging the DC algorithm with the PB equation (*50*). We used an interior dielectric constant (protein) of 1 and an exterior value (water) of 80. Further details of the DC calculations are given elsewhere (*42*, *43*).

The dispersion energy contribution, E_{disp}, was computed using an empirical formula that has been introduced by Elstner et al. (*51*) in order to extend their approximate density functional theory (DFT) method (*52*) for the description of dispersive interactions, which are normally neglected in both the DFT and semiempirical QM methods. The E_{disp} expression consists basically of a C_6/R^6 term, which is appropriately

damped for short R distances. The corresponding C_6 coefficients for each pair of interacting atoms are calculated from experimental atomic polarizabilities (*53*). We used the same parameters for C, N, O, S, and H and combination rules as those described by Elstner et al. (*51*). For Zn and Ca, their C_6 parameters were derived following similar prescriptions (*51*) and from the atomic polarizabilities of Zn^{2+} and Ca^{2+}, respectively, as evaluated at the MP2/cc-pVTZ level of theory. In a previous work (*54*), we showed that the semiempirical PM3 method complemented with the E_{disp} term is capable of reproducing fairly well the interaction energies between pairs of hydrophobic residues, as evaluated by high level correlated ab initio calculations (*55*).

To calibrate the performance of the semiempirical PM3 Hamiltonian, we examined a formal Ca^{2+} exchange process between two cluster models (~200 atoms) representing the Ca_1 and Ca_2 sites in the MMP-2 enzyme using both the PM3 method and a more sophisticated DFT level of theory. We found that PM3 predicts relative free energies for the model process comparable (±2 kcal/mol) to those predicted by the DFT method. Full details of these validation calculations are reported in the Supporting Information.

RESULTS AND DISCUSSION

Coordination Environment of the Structural Metal Ions. To represent the zinc ions, we employed a bonded approach that basically fixes the coordination sphere around Zn_1 and Zn_2. In contrast, the nonbonded representation used to model the calcium ions provides a more flexible environment that was characterized by computing the average Ca−ligand (Ca−L) distances along the different trajectories (see Table S1 in the Supporting Information). Thus, we found that the average Ca_1−L distances are in good agreement with the values observed in the initial crystal structure, the main difference arising in the interaction with the Asp_{185} residue. In the 1CK7 structure, the backbone carbonyl group of Asp_{185} is coordinated to the Ca_1 ion (2.9 Å) and the Asp_{185} side chain interacts with a sulfonate group that is encircled by the propeptide (not included in our simulations). In contrast, our simulations show that Ca_1 interacts with the Asp_{185} side chain in solution and that this interaction modulates the solvent accessibility to the Ca_1 site. According to the radial distribution of solvent molecules, one water molecule is located in the first coordination shell of Ca_1 in those trajectories presenting a stable $Ca_1\cdots Asp_{185}$ (~2.6 ± 0.1 Å) contact, whereas two water molecules can access to the Ca_1 site when the $Ca_1\cdots Asp_{185}$ contact is destabilized (~3.1 ± 0.8 Å). Concerning the Ca_2 site, we found that the Ca_2−L interactions (Glu_{166}-O$\epsilon\cdots Ca_2$, Gly_{202}-O$\cdots Ca_2$, and Asp_{204}-O$\delta\cdots Ca_2$) tend to be shorter in solution with respect to those in the initial crystal structure and the Ca^{2+} ion remains partially solvent accessible (one water molecule, also observed in the initial crystal structure, is located in the first coordination sphere). Finally, the Ca_3 ion presents four stable contacts with protein residues (Asp_{134}-Oδ1, Asp_{134}-Oδ2, Asp_{209}-O, and Glu_{211}-O; see Table S1) and turned out to be the most solvent-accessible metal ion (up to four water molecules can bind to Ca_3).

Structure of the Catalytic Domain. Figure 2 shows the superposition of the averaged MD structures, as obtained from the last 1 ns from each trajectory, onto the 1CK7 crystal

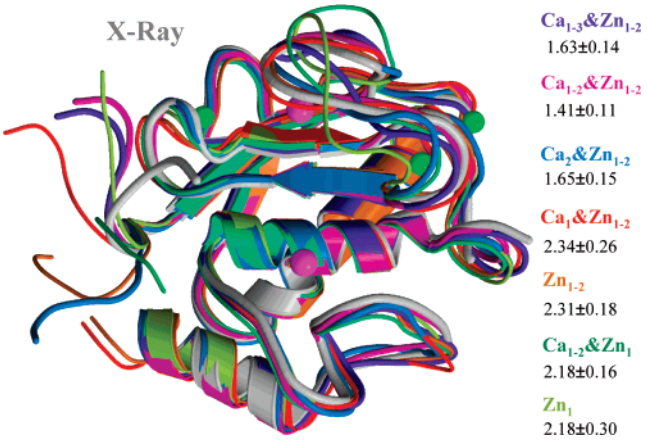

FIGURE 2: Superposition of the average structures (last 1 ns) obtained for each simulation onto the initial 1CK7 X-ray structure (in gray). The metal ions placed in the catalytic domain along each trajectory are shown as CPK spheres (zinc in magenta and calcium in green). RMSD values of the backbone atoms are given in Å.

structure. The Ca_{1-2}&Zn_{1-2} simulation, which corresponds to the configuration observed in the 1CK7 X-ray structure, is characterized by the lowest root mean squared deviation (RMSD) value. From Figure 2 it is clear that the overall architecture of the MMP-2 catalytic domain, as shown by the crystallographic studies, is preserved along the MD simulations. The largest deviations in the backbone positions arise in the N-terminal coil, which is clearly disordered, in the Zn/Ca S-loop, which interacts with Ca_1 and Zn_2, and in the $\beta4-\beta5$ connecting loop, which contacts with Ca_2. In contrast, the secondary structural elements are well maintained all along the different simulations (see below). These observations are further confirmed by segregation of the RMSD and the root mean squared flexibility (RMSF) values into different structural elements (see Table S2). It is interesting to note that the conformational variability of the MMP-2 catalytic domain predicted by our 10 ns MD simulations is in qualitative agreement with the NMR and the high-resolution X-ray structures for the MMP-12 enzyme (*7*). Thus, only some loop regions of MMP-12 are subject to backbone mobility on the $10^{-5}-10^{-9}$ s time scale according to NMR data. Moreover, these loops have been observed as "frozen" in different crystalline environments, suggesting thus that flexibility of the MMPs can be underestimated by inspection of a single X-ray or NMR structure (*7*).

In general, the loss of Ca_2 and/or Zn_2 makes the MMP-2 catalytic domain adopt a less compact structure. Thus, the average values of the radius of gyration and the solvent-accessible surface area (SASA) increase upon metal removal by 0.3−0.4 Å and 200−500 Å^2 with respect to those values corresponding to the Ca_{1-2}&Zn_{1-2} simulation (15.24 ± 0.05 Å, 9223 ± 124 Å^2). We also computed the SASA values for the four tryptophan residues located in the MMP-2 catalytic domain (see Table S3). These tryptophan residues are located in the N-terminal coil (Trp_{119}), the α1-helix (Trp_{151}), the Zn/Ca S-loop (Trp_{176}), and the fibronectin-replacing loop (Trp_{213}), with Trp_{176} presenting the largest fluctuation in its SASA value across the different simulations.

To get insight into the influence of the metal ion content on the local conformation and relative orientation of the secondary structure elements (α-helices, β-sheet, and loop

regions), we carefully analyzed the stability of the polar interactions that hold the internal conformation of the structural elements and/or interconnect them. We found that the main H-bond contacts characterizing the α-helices and the *β*-sheet are equally stable in all of the simulations. Thus, the absence of Zn_2 and/or Ca_{1-3} does not significantly perturb the conformation of the secondary structure elements. Moreover, the H-bond interactions between the α-helices, the *β*-sheet, and several loop regions are also maintained, and therefore, the relative orientation within the active site of the secondary structure elements is conserved. This is in agreement with intrinsic protein fluorescence and circular dichroism experiments showing that calcium binding to the catalytic domain is associated with changes in tertiary, but not in secondary, structure (*19*).

The loop regions that do not interact with the metal ions display H-bond contacts that are also well maintained along the different simulations. For example, the α1−*β*2 connecting loop establishes stable contacts with several sites at the α1- and α3-helices. The long Ω-loop presents several H-bond contacts (Met_{409}···Phe_{405}, Leu_{411}···Gly_{406}, His_{403}···Leu_{420}, Leu_{420}···Asp_{437}, Tyr_{445}···Met_{409}, and Ser_{414}···Met_{421}) that contribute to maintain its conformation and relative position within the MMP-2 catalytic domain. Most of the polar interactions stabilizing the Ω-loop are not perturbed by the Zn/Ca content of the catalytic domain although an important exception arises in the Ala_{419}···Thr_{426} H-bond (see below).

The *β*2−*β*3 connection loop, which binds Ca_2, gives stable contacts with several sites at the *β*1-strand (Thr_{125}···Asp_{168}, Arg_{127}···Gly_{165}, and Ile_{162}···Tyr_{126}) that contribute to define the global conformation and relative orientation of the loop. Most remarkably, these interactions are not perturbed by the removal of Ca_2. In contrast, the position of the *β*4−*β*5 connection loop is more sensitive to the absence of the metal ion as this protein region does not form stable contacts when Ca_2 is removed. On the other hand, the initial crystal structure shows that the long and solvent-exposed Zn/Ca S-loop (from Arg_{175} to Leu_{191}) establishes only a few contacts with the loops connecting the catalytic and the fibronectin domains (e.g., Arg_{175}···Asp_{210}, Asp_{188}···Glu_{211}). During the MD simulations, the Arg_{175}···Asp_{210} salt bridge is replaced by the Arg_{175}···Asp_{209} contact, but this interaction is lost when Ca_1 is removed or Ca_3 is present. Other H-bond contacts among residues of the S-loop (His_{178}-NδH···O-Arg_{175}, Phe_{184}-NH···O-Trp_{176}, and Tyr_{182}-NH···Oδ-Asp_{180}) seem important to keep the internal S-like conformation. Some of these residues (His_{178}, Asp_{180}, Glu_{211}) are coordinated to Zn_2 or Ca_1, and their H-bond contacts with other residues become clearly less stable (from 100% to 0−30% of occupancy) when the metal atoms are removed. However, the Phe_{184}-NH···O-Trp_{176} intraloop contact only disappears along the Ca_{1-3}&Zn_{1-2} and Ca_{1-2}&Zn_1 trajectories. Altogether, it seems that the lack of additional contacts with other structural elements determines that the presence of the metal ions is indispensable to stabilize the conformation and relative orientation of the Zn/Ca S-loop.

From all of the structural analyses of the MD simulations presented above, we conclude that (a) the secondary structure elements and their relative position are hardly affected by the loss of the noncatalytic metal ions (Zn_2 and/or Ca_{1-3}) and (b) the "structural role" commonly assigned to these ions mainly consists of restraining the conformation of those solvent-exposed loop regions (*β*4−*β*5 connection loop and S-loop) that cannot interact with other structural elements of the MMP-2 catalytic domain unless the metal ions are present. Nevertheless, we will see now that the average positioning and dynamics of these important loops can, in turn, modulate the accessibility of the MMP-2 active site.

Scheme 1

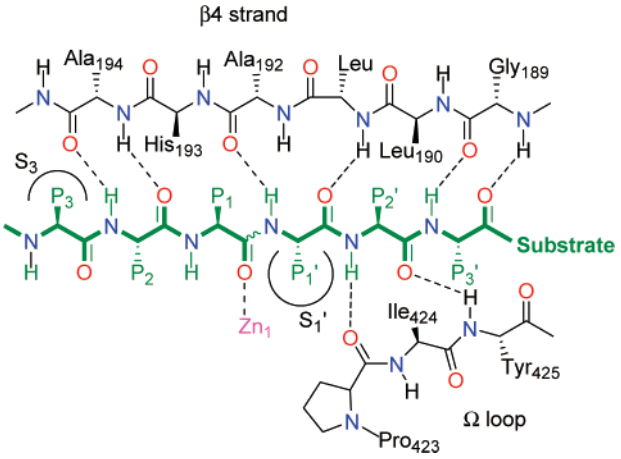

Accessibility to the Active Site Cleft. The active site of the MMPs is located in a shallow cleft that extends horizontally across the molecule and separates a smaller "lower subdomain" from the larger "upper subdomain". The cleft is bordered by the second half of the Zn/Ca S-loop, the *β*4-strand, the *β*4−*β*5 connecting loop (upper subdomain), and the Ω-loop in the lower subdomain (see Figure 1). The crystal structures of several MMP enzymes bound to different types of inhibitors suggest that peptide substrates align in an extended manner in the active site groove interacting with the so-called S_3−S_3' subsites of the catalytic domain (*8*). In these subsites, the peptides could give H-bond contacts with several main chain atoms from the S-loop (Gly_{189}-O, Leu_{191}-N), the *β*4-strand (Ala_{192}-N, Ala_{192}-O, Ala_{194}-N, Ala_{194}-O), and the Ω-loop (Pro_{423}-O, Tyr_{425}-N), adopting thus a *β*-sheet structure (see Scheme 1). In addition, two hydrophobic areas are located in the S_3 and S_1' subsites of the active site. In the MMP-2 enzyme, the S_3 pocket is built up by the Tyr_{182} (Zn/Ca S-loop), the His_{193}, and the Phe_{195} (*β*4-strand) side chains and is best suited for the binding of proline residues. The S_1' site is designed for accommodating long hydrophobic side chains from the ligands and is formed by residues from the S-loop (Leu_{191}), the α2-helix (Leu_{399}, Val_{400}, His_{403}), and the Ω-loop (Ala_{419}, Pro_{423}, Ile_{424}, Tyr_{425}) (*8*).

Clearly, the accessibility of the S_3−S_3' binding sites could modulate the affinity between the MMPs and their peptide substrates or inhibitors, affecting thus the binding process. To find out to what extent the presence of the structural metal ions can influence the accessibility of the above-described anchorage points, we computed the radius of accessibility (r_{acc}) for selected backbone and side chain groups located in the active site cleft (see Figure 3). The results are presented in Table 1.

Data in Table 1 clearly show that the removal of Ca_1 from the Zn/Ca S-loop reduces significantly the accessibility of important anchorage points located in the *β*4-strand. For instance, the r_{acc} value of the Ile_{191}-N atom lowers from 2.07 ± 0.24 Å for the Ca_{1-2}&Zn_{1-2} trajectory to 1.29 ± 0.53 and 1.04 ± 0.42 Å for the Ca_2&Zn_{1-2} and Zn_{1-2} simulations,

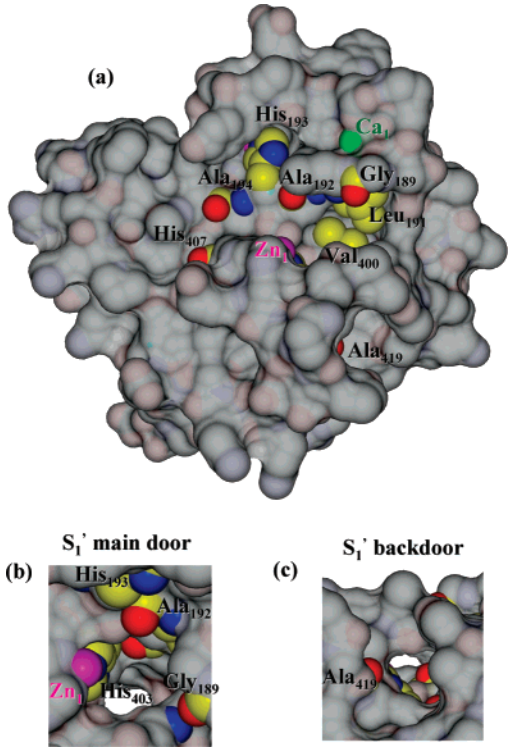

FIGURE 3: (a) Molecular surface representation of the MMP-2 enzyme in its typical orientation showing the substrate binding sites (in CPK) whose accessibility is computed. (b, c) Views of the main door and backdoor to the S_1' channel, respectively.

respectively. On the other hand, the presence of Ca_2 and Zn_2 mainly influences the conformation of the S_3 binding site. Removal of Ca_2 and/or Zn_2 increases the accessibility to the His_{193} side chain (from 4.22 ± 0.51 Å along the $Ca_{1-2}\&Zn_{1-2}$ simulation to 5.78 ± 0.41 and 5.40 ± 0.70 Å for the $Ca_1\&Zn_{1-2}$ and $Ca_{1-2}\&Zn_1$ trajectories, respectively) that, together with the Tyr_{182} and Phe_{195} side chains, delimitates the S_3 hydrophobic pocket. To further characterize the S_3 hydrophobic pocket, we present in Table 2 the average distances and angles between the center of mass of the aromatic rings of the Tyr_{182}, His_{193}, and Phe_{195} residues computed for the different simulations. The relative position of the Tyr_{182}, His_{193}, and Phe_{195} side chains fluctuates quite pronouncedly upon removal of Ca_2 and/or Zn_2 (see standard deviations in Table 2), thus destabilizing the internal conformation of the S_3 pocket. The binding of Ca_3 also contributes to destabilize the S_3 hydrophobic pocket (see Table 2).

In the crystal structures of the MMP-2 enzyme, the hydrophobic S_1' subsite is a channel that connects a main entrance located adjacent to the catalytic Zn_1 site in the active site groove with an alternative passageway (backdoor) encircled by residues from the Ω-loop (see Figure 3). The r_{acc} values collected in Table 1 are useful to characterize the structural and dynamical properties of this important region of the MMP-2 enzyme. Thus, the Pro_{423}-CO and Tyr_{425}-N groups, which are located near the Zn_1 site and can be involved in H-bond interactions with the backbone of substrate molecules, are quite accessible in all of the simulations (3.5−5.6 and 2.6−3.4 Å, respectively). Similarly, the His_{403} side chain, which is placed at the beginning of the S_1' channel, is reachable by relatively large probes (2.0−2.6 Å) in the different configurations. For the Leu_{399}-CO and Ala_{419}-CO carbonyl groups placed at the Ω-loop backdoor, however, their average r_{acc} values lie within a 1.3−2.0 Å interval, and some of them are clearly lower than that of a typical water probe radius (1.4 Å) as in the $Ca_{1-2}\&Zn_1$ configuration. To better characterize the structural fluctuations of the S_1' channel, the accessibility of the Val_{400} side chain was computed by blocking alternatively the main door and the backdoor as described in Materials and Methods. The corresponding r_{acc} values of Val_{400} in Table 2 show that its accessibility through the main entrance is large (2.0−2.5 Å) in all of the configurations. In contrast, the accessibility of Val_{400} through the Ω-loop backdoor presents mean r_{acc} values within the range of 0.8−1.2 Å for the $Ca_{1-3}\&Zn_{1-2}$, $Ca_2\&Zn_{1-2}$, $Ca_1\&Zn_{1-2}$, Zn_{1-2}, and $Ca_{1-2}\&Zn_1$ configurations. In these configurations, the bottom region of the S_1' hydrophobic pocket is effectively closed, impeding thus the traffic of water molecules (see Figure 4). Interestingly, the Ω-loop backdoor is open wide enough for passage of water molecules in the reference configuration, $Ca_{1-2}\&Zn_{1-2}$, and in the Zn_1 model lacking all of the structural metals, as demonstrated by the computed Val_{400} r_{acc} values of 1.75 ± 0.25 and 1.61 ± 0.31 Å, respectively. Moreover, several water transits through the Ω-loop backdoor were confirmed visually in the $Ca_{1-2}\&Zn_{1-2}$ and Zn_1 models (see Figure 4).

Table 1: Radius of Accessibility (Å) of Important Anchorage Points Located in the Binding Site Cleft of the MMP-2 Catalytic Domain

	$Ca_{1-3}\&Zn_{1-2}$	$Ca_{1-2}\&Zn_{1-2}$	$Ca_2\&Zn_{1-2}$	$Ca_1\&Zn_{1-2}$	Zn_{1-2}	$Ca_{1-2}\&Zn_1$	Zn_1	$Ca_{1-2}\&Zn_{1-2}$-fibronectin
Gly_{189} CO	4.22 ± 1.25	4.19 ± 0.99	5.34 ± 0.91	3.87 ± 0.92	4.12 ± 1.10	4.68 ± 0.90	5.46 ± 0.75	4.70 ± 0.99
Leu_{191} N	2.53 ± 0.39	2.07 ± 0.24	1.29 ± 0.53	2.05 ± 0.26	1.04 ± 0.42	2.49 ± 0.54	1.77 ± 0.60	2.74 ± 0.29
Leu_{191}	2.77 ± 0.39	2.09 ± 0.26	3.52 ± 0.48	2.36 ± 0.42	2.77 ± 0.34	3.16 ± 0.63	3.46 ± 0.77	2.87 ± 0.34
Ala_{192} N	2.07 ± 0.25	1.98 ± 0.21	1.48 ± 0.36	1.99 ± 0.20	1.49 ± 0.31	1.96 ± 0.29	1.68 ± 0.30	2.28 ± 0.28
Ala_{192} CO	2.49 ± 0.40	2.66 ± 0.43	2.67 ± 0.81	2.34 ± 0.32	2.31 ± 0.67	2.39 ± 0.46	3.47 ± 0.71	2.72 ± 0.43
His_{193}	5.92 ± 0.18	4.22 ± 0.51	5.78 ± 0.41	3.27 ± 0.46	4.92 ± 0.76	5.40 ± 0.70	5.88 ± 0.36	4.07 ± 0.51
Ala_{194} N	2.45 ± 0.48	2.32 ± 0.37	2.17 ± 0.26	1.81 ± 0.39	1.85 ± 0.42	2.11 ± 0.50	1.56 ± 0.51	2.21 ± 0.24
Ala_{194} CO	5.96 ± 0.20	4.48 ± 0.67	5.70 ± 0.65	3.53 ± 0.61	5.11 ± 0.80	5.55 ± 0.81	3.94 ± 1.08	4.19 ± 0.73
Leu_{339} CO	1.71 ± 0.44	1.86 ± 0.29	1.44 ± 0.58	1.73 ± 0.41	1.34 ± 0.63	1.33 ± 0.44	1.87 ± 0.19	1.93 ± 0.29
His_{403}	2.58 ± 0.34	2.02 ± 0.22	2.76 ± 0.25	2.07 ± 0.31	2.62 ± 0.28	2.78 ± 0.45	2.63 ± 0.32	2.56 ± 0.29
His_{407} CO	2.72 ± 0.49	2.42 ± 0.32	2.57 ± 0.45	1.91 ± 0.59	2.18 ± 0.54	2.60 ± 0.43	2.50 ± 0.50	2.03 ± 0.39
Ala_{419} CO	1.50 ± 0.37	2.18 ± 0.26	1.52 ± 0.32	1.54 ± 0.35	1.47 ± 0.58	1.10 ± 0.16	1.99 ± 0.38	2.21 ± 0.34
Pro_{423} CO	5.39 ± 0.93	3.47 ± 1.37	5.37 ± 0.83	5.04 ± 1.06	5.47 ± 0.75	5.58 ± 0.95	5.50 ± 0.62	5.00 ± 1.09
Tyr_{425} N	3.19 ± 0.57	2.91 ± 0.64	3.34 ± 0.62	2.63 ± 0.69	3.05 ± 0.53	3.39 ± 0.56	3.26 ± 0.71	3.14 ± 0.52
Val_{400} (S_1')[a]	2.35 ± 0.32	1.95 ± 0.27	2.49 ± 0.25	1.94 ± 0.26	2.36 ± 0.30	2.57 ± 0.50	2.16 ± 0.28	2.48 ± 0.22
Val_{400} (Ω)[b]	1.16 ± 0.42	1.75 ± 0.25	0.98 ± 0.21	1.18 ± 0.32	1.06 ± 0.51	0.78 ± 0.23	1.61 ± 0.31	1.67 ± 0.27

[a] With the backdoor opening blocked (see text for details). [b] With the S_1' main door blocked (see text for details).

Table 2: Average Values of Distances (Å) and Angles (deg) Involving Specific Protein Atoms or the Center of Mass (CM) of Side Chains Located in the S_3 and S_1' Hydrophobic Sites

	$Ca_{1-3}\&Zn_{1-2}$	$Ca_{1-2}\&Zn_{1-2}$	$Ca_2\&Zn_{1-2}$	$Ca_1\&Zn_{1-2}$	Zn_{1-2}	$Ca_{1-2}\&Zn_1$	Zn_1	$Ca_{1-2}\&Zn_{1-2}$-fibronectin
				S_3 Pocket				
CM(Tyr_{182})···CM(His_{193})	7.45 ± 1.56	5.80 ± 0.39	6.92 ± 0.44	5.76 ± 0.38	6.57 ± 0.55	6.33 ± 1.79	9.56 ± 3.55	5.79 ± 0.39
CM(Tyr_{182})···CM(His_{195})	7.91 ± 2.00	5.81 ± 0.55	5.82 ± 0.62	7.03 ± 1.56	7.56 ± 1.66	8.21 ± 2.66	11.40 ± 2.10	5.87 ± 0.54
CM(His_{193})···CM(Phe_{195})	6.75 ± 0.66	6.75 ± 0.64	5.56 ± 0.62	8.42 ± 1.83	8.11 ± 1.87	6.92 ± 1.06	6.79 ± 1.69	7.00 ± 0.52
CM(His_{193})···CM(Tyr_{182})··· CM(Phe_{195})	53.9 ± 10.8	71.3 ± 8.7	50.7 ± 6.6	81.2 ± 13.5	69.0 ± 12.0	59.3 ± 17.3	35.2 ± 12.1	74.2 ± 8.2
				S_1' Channel (Main Door)				
Zn_1···CM(Leu_{191})	10.17 ± 0.52	10.35 ± 0.44	9.94 ± 0.68	10.54 ± 0.62	10.79 ± 0.56	10.74 ± 0.61	9.73 ± 0.64	10.26 ± 0.43
Zn_1···Ala_{192}-O	6.96 ± 0.62	6.50 ± 0.46	6.44 ± 0.39	6.27 ± 0.52	6.43 ± 0.38	6.99 ± 0.55	6.73 ± 0.56	6.40 ± 0.36
Zn_1···Pro_{423}-O	6.10 ± 0.63	5.58 ± 0.73	6.18 ± 0.64	6.17 ± 0.56	6.39 ± 0.66	6.28 ± 0.55	5.75 ± 0.76	5.46 ± 0.70
Zn_1···Tyr_{425}-N	8.90 ± 0.55	8.58 ± 0.48	8.93 ± 0.55	8.87 ± 0.46	8.98 ± 0.51	9.20 ± 0.45	8.52 ± 0.65	8.44 ± 0.55
				S1′ Channel (Backdoor)				
Ala_{419}-O···CM(Leu_{420})	5.78 ± 0.11	5.80 ± 0.12	5.79 ± 0.12	5.79 ± 0.12	5.80 ± 0.12	5.76 ± 0.12	5.81 ± 0.12	5.79 ± 0.13
Ala_{419}-O···Thr_{426}-O	5.60 ± 0.67	7.65 ± 0.65	5.68 ± 0.52	5.72 ± 0.58	6.44 ± 0.91	5.68 ± 0.31	6.78 ± 0.89	8.76 ± 1.08
CM(Leu_{420})···Thr_{426}-O	8.42 ± 0.76	8.00 ± 0.58	7.27 ± 0.84	7.66 ± 0.66	8.60 ± 0.75	8.76 ± 0.52	7.99 ± 0.66	10.18 ± 1.48

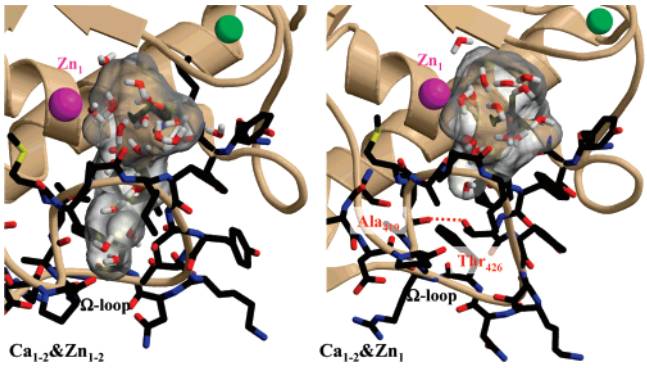

FIGURE 4: Representative snapshots of the MMP-2 catalytic domain during the $Ca_{1-2}\&Zn_{1-2}$ and $Ca_{1-2}\&Zn_1$ simulations showing the S_1' backdoor encircled by several Ω-loop residues (represented in sticks). The 1.4 Å internal molecular surface of the S_1' site that, in turn, is defined by the 2.5 Å probe-excluded region (see text for details) and the water molecules contained within or touching the internal surface are also shown. In the $Ca_{1-2}\&Zn_1$ simulation, the S_1' channel is blocked by the Ala_{419}-CO···HOγ -Thr_{426} H-bond.

To characterize the internal geometry of the S_1' site, we also computed the mean values of the distances among several groups located in the vicinity of the main entrance (see Table 2). The values in Table 2 point out that the main entrance to the S_1' site is not significantly affected by the metal content of the catalytic domain, in consonance with the r_{acc} values. On the other hand, we found that the blocking of the Ω-loop backdoor observed in several trajectories can be traced back to the formation of an H-bond contact between the Ala_{419}-CO group and the Thr_{426} side chain, both located in the Ω-loop. For example, in the $Ca_{1-2}\&Zn_1$ configuration, the Ala_{419}-CO···HOγ-Thr_{426} H-bond has 100% of abundance and the Ω-loop passageway to the S_1' site is very narrow, the corresponding Val_{400} r_{acc} value being only 0.78 ± 0.23 Å. Reciprocally, when the Ala_{419}-CO···HγO-Thr_{426} H-bond is not present, as in the $Ca_{1-2}\&Zn_{1-2}$ model, the Ω-loop backdoor is widely open. The visual inspection of the S_1' hydrophobic site in different MD snapshots revealed that the Ala_{419}···Thr_{426} contact disrupts the channel and diminishes the size of the cavity (see Figure 4).

Finally, it may be interesting to note that, when the Zn_2, Ca_1, and Ca_2 ions are bound to the catalytic domain, all of he important binding sites have accessibility values within the 2−3 Å range. Furthermore, in the $Ca_{1-2}\&Zn_{1-2}$ model, the standard deviations of the r_{acc} values in Table 1 and those of the important interatomic distances in Table 2 are quite moderate, suggesting thus that the presence of the structural ions contributes to make the structure and dynamics of the MMP-2 enzyme compatible with spontaneous access of substrate molecules to the catalytic cleft.

PB Calculations. We analyzed the changes in the protein electrostatic potential for the different simulations. As expected, the loss of *all* of the structural metal ions has a large impact on the global electrostatic properties of the catalytic domain (see Figure S2). More specific effects were observed upon removal of Ca_1 and/or Ca_2, which results in a more negative electrostatic potential in the region close to the catalytic zinc ion. This local concentration of negative electrostatic potential could perturb substrate binding or catalysis.

Energetic Analyses of the MD Trajectories. Table 3 contains the average values of the energetic terms that are combined to estimate the PM3-PBSA free energy for the various MMP-2 configurations. The evolution of the free energies over the 8 ns of production time remained stable so that mean values were then estimated to within a standard error of about 3−4 kcal/mol.

From the average *G* values in Table 3, the relative stability of the $Ca_1\&Zn_{1-2}$ and $Ca_2\&Zn_{1-2}$ states can be assessed directly. Thus, it turns out that the removal of the Ca_1 ion is much more favorable than the loss of Ca_2 by around 40 kcal/mol. The large magnitude of this energy difference allows us to safely assign the Ca_1 and Ca_2 sites as low-affinity and high-affinity Ca^{2+} binding sites in the catalytic domain of the MMP-2 enzyme.

On the other hand, the relative stability of all of the MMP-2 configurations with respect to the reference $Ca_{1-2}\&Zn_{1-2}$ configuration can be estimated by considering the free energy change for the metal dissociation processes connecting formally the different MMP-2 states (e.g., $Ca_{1-2}\&Zn_{1-2} \rightarrow Ca_1\&Zn_{1-2} + Ca^{2+}{}_{aq}$). Combining the empirical thermodynamic data for the isolated Ca^{2+} and Zn^{2+} ions in solution (*56*) with the protein *G* values in Table 3, it turns out that the most stable model would be the $Ca_{1-2}\&Zn_{1-2}$ one, in which the Ca_1, Ca_2, and Zn_2 sites are occupied. Inspection of the free energy components in Table 3 suggests that the larger stability of the $Ca_{1-2}\&Zn_{1-2}$ configuration is mainly

Table 3: PM3-Based Free Energy Components of the Protein Ion Configurations for the Catalytic Domain of the MMP-2 Enzyme[a]

system	E_{disp}	H	ΔG_{solv}	G_{total}
$Ca_{1-2}\&Zn_{1-2}$	−1419.0 (1.3)	−8608.8 (9.0)	−1908.9 (9.2)	−11936.7 (3.2) [0]
$Ca_2\&Zn_{1-2}$	−1421.6 (1.7)	−8423.4 (9.9)	−2172.5 (11.3)	−12017.6 (3.6) [9]
$Ca_{1-2}\&Zn_1$	−1389.9 (1.7)	−8451.8 (12.8)	−2270.2 (12.2)	−12112.0 (4.7) [11]
Zn_1	−1399.6 (2.4)	−7906.0 (8.9)	−2971.4 (9.1)	−12277.1 (3.7) [25]
Zn_{1-2}	−1401.9 (1.8)	−8415.4 (8.8)	−2266.8 (8.7)	−12084.3 (3.2) [31]
$Ca_1\&Zn_{1-2}$	−1395.1 (1.7)	−8499.1 (13.3)	−2082.8 (14.0)	−11977.0 (2.9) [49]
$Ca_{1-3}\&Zn_{1-2}$	−1423.2 (1.8)	−8443.3 (11.0)	−1927.7 (10.9)	−11794.3 (2.9) [53]
Zn^{2+}		665.0[b]	−467.3[c]	186.2[d]
Ca^{2+}		460.2[b]	−359.7[c]	89.5[a]

[a] Standard error of the mean values is given in parentheses. Relative differences of the mean values (ΔG) with respect to the $Ca_{1-2}\&Zn_{1-2}$ ones are in brackets. [b] From experimental data: gas-phase heat of formation and ionization potential of Zn/Ca. [c] From thermochemical absolute hydration free energies. [d] Including gas-phase absolute entropy of Zn/Ca.

due to stronger intraprotein contacts accounted for by the enthalpy term. This is in consonance with the structural analyses that characterize the $Ca_{1-2}\&Zn_{1-2}$ as the most compact model of the MMP-2 catalytic domain in solution. Therefore, we believe that the joint consideration of the previous experimental data and the present theoretical results supports the assignation of the $Ca_{1-2}\&Zn_{1-2}$ model as the most likely configuration of the MMP-2 catalytic domain provided that the appropriate concentration of Ca^{2+} and Zn^{2+} is present in solution.

On the basis of the relative ΔG values in Table 3, the following configurations, $Ca_{1-3}\&Zn_{1-2}$, $Ca_1\&Zn_{1-2}$, Zn_{1-2}, and Zn_1, are very unlikely to represent the native form of the MMP-2 enzyme in solution because their relative free energy differences with respect to $Ca_{1-2}\&Zn_{1-2}$, which are in the range of +25−53 kcal/mol, are much larger than the statistical imprecision of the individual G values. On the other hand, it is also clear that the $Ca_2\&Zn_{1-2}$ and $Ca_{1-2}\&Zn_1$ configurations, which arise from the dissociation of the Ca_1 and Zn_2 ions in the $Ca_{1-2}\&Zn_{1-2}$ state, respectively, could be energetically accessible from the $Ca_1\&Zn_{1-2}$ state as their corresponding ΔG differences are not far from the fluctuations of the mean free energies (see Table 3). The loss of the Zn_2 ion leading to the $Ca_{1-2}\&Zn_1$ state has moderate structural and energetic effects since the remaining Ca_1 can stabilize the long S-loop at least partially. Similarly, the Zn_2 ion interacts closely with the S-loop along the $Ca_2\&Zn_{1-2}$ trajectory after the removal of the Ca_1 ion. Therefore, we conclude that both the Ca_1 and Zn_2 sites would correspond to low-affinity metal binding sites in the MMP-2 enzyme.

Fibronectin-Type Domains. To evaluate the influence of the three fibronectin modules (see Figure 1) on the structure of the catalytic domain, we computed the MD trajectory $Ca_{1-2}\&Zn_{1-2}$-fibronectin that contains two Ca^{2+} and two Zn^{2+} ions in the active site. The resulting backbone RMSD values for each fibronectin-type domain (1.38 ± 0.25, 1.32 ± 0.1, and 1.77 ± 0.33 Å, respectively) show that the deviation from the initial X-ray structure is more accentuated for the third fibronectin module. This can be related with the loss of some contacts observed in the solid-state structure between the third fibronectin domain and the propeptide domain (which is not included in our simulations). For example, the Phe_{37} side chain in the propeptide is located into the hydrophobic pocket of the third fibronectin domain, and there are also H-bond ($Ile_{35}\cdots Gly_{367}$) and salt bridge ($Asp_{40}\cdots Arg_{368}$) interactions between both domains.

In the initial X-ray structure, the fibronectin modules establish several polar interactions with the catalytic domain (either through direct H-bond contacts or mediated by one solvent molecule) that resulted quite stable along the $Ca_{1-2}\&Zn_{1-2}$-fibronectin MD simulation. For example, the first and second fibronectin domains interact with the $\beta 1-\alpha 1$ connecting loop through four stable H-bond contacts: Gln_{219}-NϵH···O-Asp_{134} (93%, 2.95 ± 0.16 Å), Asp_{136}-NH···O-Val_{220} (99%, 3.00 ± 0.15 Å), Tyr_{232}-OηH···Oδ-Asp_{136} (88%, 2.72 ± 0.15 Å), and Thr_{335}-NH···O-Pro_{133} (97%, 2.90 ± 0.14 Å). There is also a stable contact between the $\beta 1$-strand and the second fibronectin domain (Arg_{127}-NηH···O-Thr_{311} 98%, 2.89 ± 0.15 Å) and a weaker interaction between the Zn/Ca S-loop and the third fibronectin domain (Lys_{187}-NζH···O-Val_{340} 56%, 2.92 ± 0.17 Å). In addition, several polar contacts among the three fibronectin modules contribute to stabilize their relative arrangement. For instance, the Gln_{219}, Arg_{222}, Lys_{224}, and Cys_{247} residues from the first fibronectin module establish long-lived H-bond contacts (72−98% of occupancy) with the Glu_{334}, Thr_{335}, and Ala_{336} residues located in the loop that connects the second and the third fibronectin domains.

The comparison of the $Ca_{1-2}\&Zn_{1-2}$ and $Ca_{1-2}\&Zn_{1-2}$-fibronectin trajectories shows that the presence of the fibronectin modules has only a minor influence on the overall structure and flexibility of the catalytic domain. The average values for the radius of gyration point out that the catalytic domain displays only a slightly more compact structure in the presence of the three fibronectin domains. Moreover, the RMSD and RMSF values, as well as the accessibility values of the important anchorage points, are very similar in the $Ca_{1-2}\&Zn_{1-2}$ and $Ca_{1-2}\&Zn_{1-2}$-fibronectin simulations (see Tables 1 and S2). Similarly, the internal structure and dynamics of the S_1' channel is basically the same in the two states since the above-mentioned Ω-loop backdoor is open all along the $Ca_{1-2}\&Zn_{1-2}$-fibronectin trajectory. Thus, the presence of the three fibronectin-type modules does not modify the structural properties of the catalytic domain, in agreement with the evidence provided by X-ray crystallography (*23*).

Metal Ion Content and Activity of the MMPs. As mentioned in the introduction, it has been shown that removal of Ca^{2+} ions from MMP-1 and MMP-3 generates catalytically incompetent enzymes (*18*, *21*). The presence of Ca^{2+} ions is also important in other aspects of the MMPs activity, as in the case of the activation of the pro-MMP-2 enzyme (*57*). As a matter of fact, some authors have postulated that the function of extracellular proteins, including the MMPs, could be regulated by physiologically relevant Ca^{2+} gradients (*58*). This hypothesis has gained support in a recent study

on the Ca^{2+} regulation of the tertiary structure and enzymatic activity of the human endometase/matrilysin-2 enzyme (MMP-26) (*59*). In this study, the authors have concluded that the low intracellular Ca^{2+} concentration maintains the MMP-26 enzyme in its inactive form, which can be reversibly transformed into its competent form at the higher Ca^{2+} concentration typical of extracellular conditions.

Our computational results can shed some light onto the Ca^{2+} mode of action in order to control the hydrolytic activity of the MMPs. Although the secondary structural elements are hardly affected by the presence or absence of the Ca^{2+} ions, we found that the stabilization of the important loops induced by Ca^{2+} is related with the structure and accessibility of the S_3-S_3' binding sites located along the active site groove. In this way, it turns out that the accessibility of the main binding sites for peptide substrates is modified upon removal of the structural metal ions in several manners: (a) removal of the Ca_1 ion packed between the last half of the S-loop and the β-sheet results in small r_{acc} values (1.0−1.5 Å) for the Leu_{191}-N and Ala_{192}-N atoms; (b) the presence of Ca_2 and Zn_2 seems to be essential for the correct assembling of the S_3 hydrophobic pocket; (c) the metal ion content of the catalytic domain does not perturb significantly the main entrance to the S_1' channel but has a larger impact on the back opening of the channel, which becomes a closed pocket upon removal of Zn_2, Ca_1, and/or Ca_2. We note that a relatively wide Ω-loop backdoor (>1.4 Å) could provide an efficient vent for water molecules, facilitating thus the desolvation of the active site during substrate binding. All of these structural effects associated to the removal of the Ca_{1-2} and Zn_2 ions could hinder substrate binding, thereby reducing the catalytic activity of the MMP-2 enzyme.

In summary, we have reported in this work dynamical models of the catalytic domain of the MMP-2 enzyme in aqueous solution that allowed us to characterize at the atomic level the role played by the structural metal ions, particularly in modulating the accessibility of the important binding sites. As suggested by combined NMR and high-resolution X-ray crystallography experiments (*7*), flexibility in crucial parts of the catalytic domain of the MMPs could be a requisite for substrate binding and broad substrate specificity. Therefore, our MD models could be relevant for modeling of the MMP-2 enzyme in complex with substrates and inhibitors that bind to the active site. In addition, knowledge gained in this study could be useful to better understand the inhibition of the MMPs exerted by drug molecules like the tetracycline antibiotics (doxycycline) (*60*), which do not interact with the catalytic Zn_1 site but with the structural metal centers.

ACKNOWLEDGMENT

The authors thankfully acknowledge the computer resources, technical expertise, and assistance provided by the Barcelona Supercomputing Center—Centro Nacional de Supercomputación.

SUPPORTING INFORMATION AVAILABLE

Parametrization of the zinc ions, validation calculations, Tables S1−S4, and Figures S1−S2. This material is available free of charge via the Internet at http://pubs.acs.org.

REFERENCES

1. McCawley, L. J., and Matrisian, L. (2001) Matrix metalloproteinases: they're not just for matrix anymore!, *Curr. Opin. Cell Biol. 13*, 534−540.
2. Lee, M.-H., and Murphy, G. (2004) Matrix metalloproteinases at a glance, *J. Cell Sci. 117*, 4015−4016.
3. Egeblad, M., and Werb, Z. (2002) New functions for the matrix metalloproteinases in cancer progression, *Nat. Rev. Cancer 2*, 163−176.
4. Fingleton, B. (2006) Matrix metalloproteinases: roles in cancer and metastasis, *Front. Biosci. 11*, 479−491.
5. van Meurs, J., van Lent, P., Holthuysen, A., Lambrou, D., Bayne, E., Singer, I., and van den Berg, W. (1999) Active matrix metalloproteinases are present in cartilage during immune complex-mediated arthritis: a pivotal role for stromelysin-1 in cartilage destruction, *J. Immunol. 163*, 5633−5639.
6. Bode, W., Fernandez-Catalan, C., Tschesche, H., Grams, F., Nagase, H., and Maskos, K. (1999) Structural properties of matrix metalloproteinases, *Cell. Mol. Life Sci. 55*, 639−652.
7. Bertini, I., Calderone, V., Cosenza, M., Fragai, M., Lee, Y.-M., Luchinat, C., Mangani, S., Terni, B., and Turano, P. (2005) Conformational variability of matrix metalloproteinases: Beyond a single 3D structure, *Proc. Natl. Acad. Sci. U.S.A. 102*, 5334−5339.
8. Maskos, K. (2005) Crystal structures of MMPs in complex with physiological and pharmacological inhibitors, *Biochimie 87*, 249−263.
9. Johnson, L. L., Pavlovsky, A. G., Johnson, A. R., Janowick, J. A., Man, C.-F., Ortwine, D. F., Purchase, C. F., II, White, A. D., and Hupe, D. J. (2000) A rationalization of the acidic pH dependence for stromelysin-1 (matrix metalloproteinase-3) catalysis and inhibition, *J. Biol. Chem. 275*, 11026−11033.
10. Arza, B., De Maeyer, M., Félez, J., Collen, D., and Lijnen, H. R. (2001) Critical role of glutamic acid 202 in the enzymatic activity of stromelysin-1 (MMP-3), *Eur. J. Biochem. 268*, 826−831.
11. Salowe, S. P., Marcy, A. I., Cuca, G. C., Smith, C. K., Kopka, I. E., Hagmann, W. K., and Hermes, J. D. (1992) Characterization of zinc-binding sites in human stromelysin-1: Stoichiometry of the catalytic domain and identification of a cysteine ligand in the proenzyme, *Biochemistry 31*, 4535−4540.
12. Soler, D., Nomizu, T., Brown, W. E., Chen, M., Ye, Q.-Z., Van Wart, H. E., and Auld, D. S. (1994) Zinc content of promatrilysin, matrilysin and the stromelysin catalytic domain, *Biochem. Biophys. Res. Commun. 201*, 917−923.
13. Springman, E. B., Nagase, H., Birkedal-Hansen, H., and Van Wart, H. E. (1995) Zinc content and function in human fibroblast collagenase, *Biochemistry 34*, 15713−15720.
14. Willenbrock, F., Murphy, G., Phillips, I. R., and Brocklehurst, K. (1995) The second zinc atom in the matrix metalloproteinase catalytic domain is absent in the full-length enzymes: a possible role for the C-terminal domain, *FEBS Lett. 358*, 189−192.
15. Williams, D. H., and Murray, E. J. (1994) Specific amino acid substitutions in human collagenase cause decreased autoproteolysis and reveal a requirement for a second zinc atom for catalytic activity, *FEBS Lett. 354*, 267−270.
16. Massova, I., Kotra, L. P., and Mobashery, S. (1998) Structural insight into the binding motifs for the calcium ion and the non-catalytic zinc in matrix metalloproteases, *Bioorg. Med. Chem. Lett. 8*, 853−858.
17. Andreini, C., Banci, L., Bertini, I., Luchinat, C., and Rosato, A. (2004) Bioinformatic comparison of structures and homoly-models of matrix metalloproteinases, *J. Proteome Res. 3*, 21−31.
18. Wetmore, D. R., and Hardman, K. D. (1996) Roles of the propeptide and metal ions in the folding and stability of the catalytic domain of stromelysin (matrix metalloproteinase 3), *Biochemistry 35*, 6549−6558.
19. Zhang, Y., Dean, W. L., and Gray, R. D. (1997) Cooperative binding of Ca^{2+} to human interstitial collagenase assessed by circular dichroism, fluorescence, and catalytic activity, *J. Biol. Chem. 272*, 1444−1447.
20. Lowry, C. L., McGeehan, G., and LeVine, H. (1992) Metal ion stabilization of the conformation of a recombinant 19-kDa catalytic fragment of human fibroblast collagenase, *Proteins: Struct., Funct., Genet. 12*, 42−48.
21. Housley, T. J., Baumann, A. P., Braun, I. D., Davis, G., Seperack, P. K., and Wilhelmt, S. M. (1993) Recombinant chinese hamster ovary cell matrix metalloprotease-3 (MMP-3, stromelysin-1), *J. Biol. Chem. 268*, 4481−4487.

22. Dhanaraj, V., Willians, M. G., Ye, Q. Z., Molina, F., Johnson, L. L., Ortwine, D. F., Pavlovsky, A., Rubin, J. R., Skeean, R. W., White, A. D., Humblet, C., Hupe, D. J., and Blundell, T. L. (1999) X-ray structure of gelatinase A catalytic domain complexed with a hydroxamate inhibitor, *Croat. Chem. Acta 72*, 575−591.
23. Morgunova, E., Tuuttila, A., Bergmann, U., Isupov, M., Lindqvist, Y., Schneider, G., and Tryggvason, K. (1999) Structure of human pro-matrix metalloproteinase-2: activation mechanism revealed, *Science 284*, 1667−1670.
24. Morgunova, E., Tuuttila, A., Bergmann, U., and Tryggvason, K. (2002) Structural insight into the complex formation of latent matrix metalloproteinase 2 with tissue inhibitor of metalloproteinase 2, *Proc. Natl. Acad. Sci. U.S.A. 99*, 7414−7419.
25. Feng, Y., Likos, J. J., Zhu, L., Woodward, H., Munie, G., McDonald, J. J., Stevens, A. M., Howard, C. P., De Crescenzo, G. A., Welsch, D., Shieh, H. S., and Stallings, W. C. (2002) Solution structure and backbone dynamics of the catalytic domain of matrix metalloproteinase-2 complexed with a hydroxamic acid inhibitor, *Biochim. Biophys. Acta 1598*, 10−23.
26. Cheatham, T. E. I., Cieplak, P., and Kollman, P. A. (1999) A modified version of the Cornell et al. force field with improved sugar pucker phases and helical repeat, *J. Biomol. Struct. Dyn. 16*, 845−862.
27. Aqvist, J. (1990) Ion-water interaction potentials derived from free energy perturbation simulations, *J. Phys. Chem. 94*, 8021−8024.
28. Case, D. A., Darden, T. A., Cheatham, T. E. I., Simmerling, C. L., Wang, J., Duke, R. E., Luo, R., Merz, K. M., Wang, B., Pearlman, D. A., Crowley, M., Brozell, S., Tsui, V., Gohlke, H., Mongan, J., Hornak, V., Cui, G., Beroza, P., Schafmeister, C., Caldwell, J. W., Ross, W. S., and Kollman, P. A. (2004) AMBER 8.0, University of California, San Francisco.
29. Essman, V., Perera, L., Berkowitz, M. L., Darden, T., Lee, H., and Pedersen, L. G. (1995) A smooth particle-mesh-Ewald method, *J. Chem. Phys. 103*, 8577−8593.
30. Berendsen, H. J. C., Potsma, J. P. M., van Gunsteren, W. F., DiNola, A. D., and Haak, J. R. (1984) Molecular dynamics with coupling to and external bath, *J. Chem. Phys. 81*, 3684−3690.
31. Sanner, M. F., Olson, A. J., and Spehner, J.-C. (1996) Reduced surface: an efficient way to compute molecular surfaces, *Biopolymers 38*, 305−320.
32. Tai, K., Shen, T., Börjesson, U., Philippopoulos, M., and McCammon, J. A. (2001) Analysis of a 10-ns molecular dynamics simulation of mouse acetylcholinesterase, *Biophys. J. 81*, 715−724.
33. Suárez, D., and Field, M. J. (2005) Molecular dynamics simulations of human butyrylcholinesterase, *Proteins: Struct., Funct., Bioinf. 59*, 104−117.
34. Weiner, S. J., Kollman, P. A., Case, D. A., Singh, U. C., Ghio, C., Alagona, G., Profeta, S., and Weiner, P. (1984) A new force field for molecular mechanical simulation of nucleic acids and proteins, *J. Am. Chem. Soc. 106*, 765−784.
35. Whittaker, M., Floyd, C. D., Brown, P., and Gearing, A. J. H. (1999) Design and therapeutic application of matrix metalloproteinase inhibitors, *Chem. Rev. 99*, 2735−2776.
36. Kiyama, R., Tamura, Y., Watanabe, F., Tsuzuki, H., Ohtani, M., and Yodo, M. (1999) Homology modeling of gelatinase catalytic domains and docking simulations of novel sulfonamide inhibitors, *J. Med. Chem. 42*, 1723−1738.
37. Sharp, K., and Honig, B. (1991) Electrostatic interactions in macromolecules: theory and applications, *Annu. Rev. Biophys. Biophys. Chem. 19*, 301−332.
38. Rocchia, W., Alexov, E., and Honig, B. (2001) Extending the applicability of the nonlinear Poisson-Boltzmann equation: Multiple dielectric constants and multivalent ions, *J. Phys. Chem. B 105*, 6507−6514.
39. Rappé, A. K., Casewit, C. J., Colwell, K. S., Goddard, W. A., III, and Skiff, W. M. (1992) UFF, a full periodic table force field for molecular mechanics and molecular dynamics simulations, *J. Am. Chem. Soc. 114*, 10024−10035.
40. Kollman, P. A., Massova, I., Reyes, C., Kuhn, B., Huo, S., Chong, L., Lee, M., Lee, T., Duan, Y., Wang, W., Donini, O., Cieplak, P., Srinivasan, J., Case, D. A., and Cheatham, T. E. (2000) Calculating structures and free energies of complex molecules: Combining molecular mechanics and continuum models, *Acc. Chem. Res. 33*, 889−897.
41. Gohlke, H., and Case, D. A. (2003) Converging free energy estimates: MM-PB(GB)SA studies on the protein-protein complex Ras-Raf, *J. Comput. Chem. 25*, 238−250.
42. Díaz, N., Suárez, D., and Sordo, T. L. (2006) Molecular dynamics simulations of class C β-lactamase from *Citrobacter freundii*: Insights into the base catalyst for acylation, *Biochemistry 45*, 439−451.
43. Díaz, N., Sordo, T. L., and Suárez, D. (2005) Insights into the base catalysis exerted by the DD-transpeptidase from *Streptomyces* K15: a molecular dynamics study, *Biochemistry 44*, 3225−3240.
44. Wollacott, A. M., and Merz, K. M., Jr. (2006) Development of a parametrized force field to reproduce semiempirical geometries, *J. Chem. Theory Comput. 2*, 1070−1077.
45. Yang, W., and Lee, T.-S. (1995) A density-matrix form of the divide-and-conquer approach for electronic structure calculations of large molecules, *J. Chem. Phys. 103*, 5674−5678.
46. Dixon, S. L., and Merz, K. M., Jr. (1997) Fast, accurate semiempirical molecular orbital calculations for macromolecules, *J. Chem. Phys. 107*, 879−893.
47. Wang, B., Raha, K., Liao, N., Peters, M. B., Kim, H., Westerhoff, L. M., Wollacott, A. M., van der Vaart, A., Gogonea, V., Suarez, D., Dixon, S. L., Vincent, J. J., Brothers, E. N., and Merz, K. M. J. (2005), QuantumBio Inc., State College, PA.
48. Stewart, J. J. P. (1989) Optimization of parameters for semiempirical methods I. Method, *J. Comput. Chem. 10*, 209−220.
49. Brothers, E. N., Suárez, D., Deerfield, D. W. I., and Merz, K. M. J. (2004) PM3-compatible zinc parameters optimized for metalloenzyme active sites, *J. Comput. Chem. 25*, 1677−1692.
50. Gogonea, V., and Merz, K. M., Jr. (1999) Fully quantum mechanical description of proteins in solution. Combining linear scaling quantum mechanical methodologies with the Poisson-Boltzmann equation, *J. Phys. Chem. A 103*, 5171−5178.
51. Elstner, M., Hobza, P., Frauenheim, T., Suhai, S., and Kaxiras, E. (2001) Hydrogen bonding and stacking interactions of nucleic acid base pairs: A density-functional-theory based treatment, *J. Chem. Phys. 114*, 5149−5154.
52. Elstner, M., Porezag, D., Jungnickel, G., Elsner, J., Haugk, M., Frauenheim, T., Suhai, S., and Seifert, G. (1998) Self-consistent-charge density-functional tight-binding method for simulations of complex materials properties, *Phys. Rev. B 58*, 7260−7268.
53. Miller, K. J. (1990) Additivity methods in molecular polarizability, *J. Am. Chem. Soc. 112*, 8533−8542.
54. Díaz, N., Suárez, D., and Sordo, T. L. (2006) Quantum chemical study on the coordination environment of the catalytic zinc ion in matrix metalloproteinases, *J. Phys. Chem. B 110*, 24222−24230.
55. Vondrásek, J., Bendová, L., Klusák, V., and Hobza, P. (2005) Unexpectedly strong energy stabilization inside the hydrophobic core of small protein rubredoxin mediated by aromatic residues: correlated ab initio quantum chemical calculations, *J. Am. Chem. Soc. 127*, 2615−2619.
56. Marcus, Y. (1994) A simple empirical model describing the thermodynamics of hydration of ions of widely varying charges, sizes and shapes, *Biophys. Chem. 51*, 111−127.
57. Munshi, H. G., Wu, Y. I., Ariztia, E. V., and Stack, M. S. (2002) Calcium regulation of matrix metalloproteinase-mediated migration in oral squamous cell carcinoma cells, *J. Biol. Chem. 277*, 41480−41488.
58. Maurer, P., and Hohenester, E. (1997) Structural and functional aspects of calcium binding in extracellular matrix proteins, *Matrix Biol. 15*, 569−580.
59. Lee, S., Park, H. I., and Sang, Q.-I. A. (2007) Calcium regulates tertiary structure and enzymatic activity of human endometase/matrilysin-2 and its role in promoting human breast cancer cell invasion, *Biochem. J. 403*, 31−42.
60. García, R. A., Pantazatos, D. P., Gessner, C. R., Go, K. V., Woods, V. L. J., and Villarreal, F. J. (2005) Molecular interactions between matrilysin and the matrix metalloproteinase inhibitor doxycycline investigated by deuterium exchange mass spectrometry, *Mol. Pharmacol. 67*, 1129−1136.

BI700541P